Proton deflectometry analysis in magnetized plasmas: Magnetic field reconstruction in one dimension

W. Fox [1,2,*,†] G. Fiksel [3,*] D. B. Schaeffer [2,‡] and J. Griff-McMahon [1,2]

[1]*Princeton Plasma Physics Laboratory*, Princeton, New Jersey 08543, USA

[2]*Department of Astrophysical Sciences, Princeton University*, Princeton, New Jersey 08544, USA

[3]*Center for Ultrafast Optical Science, University of Michigan, Ann Arbor*, Michigan 48109, USA

Proton deflectometry is used in magnetized high-energy-density plasmas to observe electromagnetic fields. We describe a reconstruction algorithm to recover the electromagnetic fields from proton fluence data in 1-D. The algorithm is verified against analytic solutions and applied to example data. Next, we study the role of source fluence uncertainty for 1-D reconstructions. We show that reconstruction boundary conditions can be used to constrain the source fluence profile and use this to develop a reconstruction using a specified pair of boundary conditions on the magnetic field. From these considerations, we experimentally demonstrate a hybrid mesh-fluence reconstruction technique where fields are reconstructed from fluence data in an interior region with boundary conditions supplied by direct mesh measurements at the boundary.

I. INTRODUCTION

Proton deflectometry (or radiography) [1–3] is increasingly used to observe the evolution of electric and magnetic fields in high-energy-density plasmas. This has enabled magnetic field observations in experiments ranging from compressed fields for inertial fusion energy [4] and self-generated magnetic fields in laser-solid interaction [5–7] to laboratory astrophysics measurements of Weibel instability [8], magnetic reconnection [9–12], magnetized shocks [13], and plasma dynamos [14].

The principle of the measurement, which has been discussed in Refs. [1,2], and a recent review article [3], is to use a beam of protons to map the electromagnetic fields in an experiment. A point source of protons is generated through either a laser-driven implosion of a D^{3}He-filled capsule or laser-solid interaction. The protons then stream through a region under study, where they pick up small-angle deflections from the electromagnetic fields, before propagating ballistically to a detector. The goal is to use the detected protons to infer the electromagnetic fields. Oftentimes a grid or mesh is used to break the protons into beamlets (e.g., Refs. [6,10]). This has the virtue that the beamlets can be directly located on the detector to measure the proton final positions. X rays are also generated in D^{3}He implosions, and these can be mapped simultaneously using appropriately designed detector stacks [15,16]. Since x rays are not deflected by electromagnetic fields, the x-ray beamlets provide a direct reference of the undeflected beamlet locations.

While the mesh enables a direct measurement of the proton deflections, it also sacrifices spatial resolution. To observe at higher resolution, it is also possible to take direct proton fluence images without a mesh. In this case, the proton focusing and defocusing by the electromagnetic fields leads to fluence variations on the detector, and the goal is then to reconstruct the fields which create these variations. Generating forward proton models (e.g., Ref. [11]) to compare with experimental data is straightforward, since one simply has to generate model fields and then calculate and bin proton trajectories to generate an image for comparison. A quantitative analytic theory connecting proton deflections to fluence variations was described by Kugland *et al.* [1]. Finally, and potentially most powerfully, algorithms have been developed to invert measured fluence images to obtain the experimental electromagnetic fields [2,17,18]. These inversion techniques generally involve an optimization or relaxation-type solution to the Monge-Ampère transport equation [2,17,19], whereas other algorithms have been developed that exploit the analogy between deflectometry and charged particle motion [18], or use neural networks [20].

In this article, we develop and verify a 1-D inversion algorithm to obtain 1-D field profiles from proton fluence profiles through direct integration of an ordinary differential equation (ODE). This is complementary to 2-D algorithms mentioned above [2,17,18]. The algorithm is fully nonlinear and can reconstruct for large proton deflections, as long as there are no caustics and the proton trajectories do not cross. It therefore works in the same "nonlinear injective" regime of Ref. [2]. A virtue of a 1-D algorithm is that it can run very quickly (typically <0.1 sec for a reconstruction), and therefore can be easily embedded within higher-level workflows for error analysis and parametric scans. Furthermore, several experiments, including magnetic reconnection [12], magnetized cylindrical implosions [4], or transport in magnetized

---

*These authors contributed equally to this work.

†Contact author: wfox@pppl.gov

‡Present address: Department of Physics and Astronomy, University of California - Los Angeles, Los Angeles, California 90095, USA.

plasmas [21] related to fusion concepts such as MagLIF [22] have 1-D or nearly 1-D regions which can be analyzed by this technique. Variations on this algorithm have been implemented in cylindrical geometry to analyze cylindrically symmetric expanding plasmas [23].

Next, we investigate some subtleties for 1-D reconstructions, such as the connection between the reconstruction boundary conditions and the "source" proton fluence, which is the proton fluence before it is deflected by the experimental fields. We show that reconstruction boundary conditions can be used to directly constrain the average source proton fluence. We use this result to implement arbitrary magnetic field boundary conditions for the 1-D algorithm. (Other commonly used solvers, e.g., PROBLEM [24] at the time of this writing, apply the zero-deflection boundary condition $\mathbf{B}_{\text{tangential}} = 0$.) We also explore the "integration error" introduced by error in the source fluence. We focus on error in the average level, yet the results also have implications for the more general question of source fluence nonuniformity. These results complement prior statistical analysis of source fluence uncertainties [25]. Finally, we develop and experimentally demonstrate a "hybrid" proton fluence deflectometry technique, with separate mesh and fluence regions in the same radiograph, where mesh regions provide direct measurement of magnetic field boundary conditions for the reconstruction in the fluence region.

This work is intended to be the beginning of a series of works that discuss analysis of proton data for recent experiments. The focus is on proton deflectometry with careful analysis of the various sources of measurement uncertainty, to allow quantitative statements about measured magnetic fields with error bars. A first physics analysis of magnetic reconnection experiments using this analysis technique is presented in Ref. [26]. Finally, an Appendix describes the implementation of the routines (presently in Matlab) in a package called PRADICAMENT.

II. PROTON DEFLECTIONS

In this section, we briefly review the measurement setup and basic theory of proton deflections to fix the geometry and notation to be used below. The reader is referred to Refs. [1–3] for extended discussion of the proton deflectometry theory. Figure 1 shows a typical experimental geometry. The protons emerge from a point source located at a distance L_s from the plasma under study. The detector is positioned at a distance L_d on the opposite side. (The figure is not to scale, as often $L_d \gg L_s$, in a point-magnification geometry.) As the protons travel through the plasma region, they pick up small angle deflections $\Delta\alpha$ due to electromagnetic fields. The figure shows an example magnetic geometry representative of recent experiments on laser-driven magnetic reconnection [10,12], in connection with the verification example below.

Following the development from prior work on proton deflectometry [1,2], we consider high-energy protons which only pick up small deflections $|\Delta\mathbf{V}| \ll V_p$ while propagating through the plasma, where $V_p = (2E_p/m_p)^{1/2}$ is the proton speed given the initial proton energy E_p. In this limit, the deflection is given by an integral over the straight-line
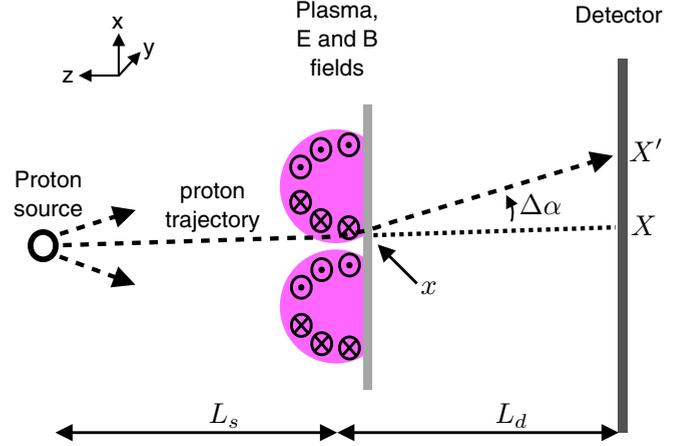
FIG. 1. Schematic of the measurement setup and coordinate system. A proton source produces a point source of high-energy protons. These stream through an experimental region, where the protons pick up deflections $\Delta\alpha$ due to electromagnetic fields, after which they propagate ballistically to a detector. An example proton crosses the plasma plane at position x, where the electromagnetic fields deflect the trajectory, causing the proton to arrive at position X' rather than X on the detector.

trajectory,

$$\Delta\boldsymbol{\alpha} = \frac{\Delta\mathbf{V}}{V_p} = \frac{e}{m_p V_p^2} \int (\mathbf{E} + \mathbf{V_p} \times \mathbf{B})_\perp \, d\ell. \quad (1)$$

The validity of this limit is extensively discussed in Refs. [1,2].

Considering the detector geometry, the proton crossing the plasma at position x arrives at the detector at position

$$\mathbf{X}' = (1 + L_d/L_s)\mathbf{x} + L_d \Delta\boldsymbol{\alpha}(\mathbf{x}). \quad (2)$$

It is convenient to work just in the coordinate system of the plasma plane, so we use the "final" proton position mapped back to the plasma plane, $\mathbf{x}' = \mathbf{X}'/M$, using the magnification $M = (1 + L_d/L_s)$, so that

$$\mathbf{x}' = \mathbf{x} + \frac{L_s L_d}{L_s + L_d} \Delta\boldsymbol{\alpha} \quad (3)$$

$$= \mathbf{x} + \boldsymbol{\xi}(\mathbf{x}), \quad (4)$$

introducing the deflection $\boldsymbol{\xi}(\mathbf{x})$. With this definition,

$$\boldsymbol{\xi}(\mathbf{x}) = K_B^{-1} \int d\boldsymbol{\ell} \times \mathbf{B} + K_E^{-1} \int \mathbf{E}_\perp \, d\ell, \quad (5)$$

using the deflection "rigidity" factors

$$K_B = \frac{m_p V_p}{e} \frac{L_s + L_d}{L_s L_d} \quad (6)$$

and

$$K_E = \frac{m_p V_p^2}{e} \frac{L_s + L_d}{L_s L_d}. \quad (7)$$

The units of K_B and K_E are conveniently (in SI) Tesla and V/m. However, with this formulation, the mapping can work in any consistent unit scheme, and, for example, K_B can be converted to Gauss. If $\int B_y \, dz$ is given in T-m and K_B in T, this produces a deflection ξ with units of m. The interpretation of

K_B is that, for example, given $K_B = 50$ T, for a line-integrated field $\int d\ell \times B = 50$ T-mm, the proton will be deflected 1 mm in plasma plane units.

For the present analysis, we now specialize to a 1-D geometry, with protons propagating primarily along z, and deflected *only* in the x-direction, so that we have a mapping which is the 1-D version of Eq. (4),

$$x' = x + \xi(x), \tag{8}$$

where ξ is a function of x only, given by

$$\xi(x) = K_B^{-1} \int B_y \, dz + K_E^{-1} \int E_x \, dz. \tag{9}$$

The proton fluence (defined as protons / unit area, or a similar quantity) is assumed first to have a known "initial" or "source" fluence $I_0(x)$, when the protons first reach the plasma plane. The proton deflections $x \rightarrow x'$ then map this fluence to the detector image $I(x')$. For a given magnetic field structure, one can calculate a synthetic proton fluence image, which we call I_{fwd}. To do this, one calculates many proton mappings via Eq. (8), with initial positions drawn from the source fluence profile $I_0(x)$, binning the final positions x' to determine the final fluence profile.

In 1-D, the fluence transforms according to the Jacobian of the proton mapping [1],

$$I(x') = \frac{I_0(x)}{|dx'/dx|}. \tag{10}$$

This equation holds if the magnetic field is limited in magnitude to an extent that $dx'/dx > 0$, which is equivalent to the absence of caustics in the proton image (i.e., that proton trajectories do not cross *en route* to the detector). While Eq. (10) is valid in noncaustic regimes, the forward binning technique works even in caustic regimes and is therefore more general. Reference [1] discusses caustic formation extensively and provides several examples.

Equation (10) is equivalent to a statement of conservation of protons,

$$\int_{x_1}^{x_2} I_0(x) \, dx = \int_{x_1'}^{x_2'} I(x') \, dx' \tag{11}$$

considering an integral on $[x_1, x_2]$ of the initial protons or $[x_1', x_2']$ over the final protons. A perennial subtlety of the analysis is that the fluence data $I(x')$ is "observed at" the final coordinates x' but depends on the source fluence at the initial coordinates, $I_0(x)$.

III. RECONSTRUCTION

We now develop how to reconstruct the magnetic (or alternatively electric) fields from the fluence data. The equations are the 1-D limit of prior image-fluence relations [1,2], however, with the 1-D formulation, the present method departs from the relaxation method of Refs. [2,19]. We introduce $b(x) = \int B_y \, dz$ as the line-integrated magnetic field, for brevity. Hereafter, we also assume the electric deflection is negligible so that there is a constant relation between ξ and b. For the more general case, one can analyze multiple reconstructions from various orientations [6] or with different

proton energies to separate the electric and magnetic field contributions.

To reconstruct, we determine the relationship between the mapping and the measured proton fluence $I(x')$. First, we find, using Eq. (8),

$$\frac{dx'}{dx} = 1 + \frac{d\xi}{dx}. \tag{12}$$

After substituting this in Eq. (10), and using $b = K_B \xi$, we find the following relation between b, I, and I_0,

$$\frac{db}{dx} = K_B \frac{d\xi}{dx} = K_B \left(\frac{I_0(x)}{I(x')} - 1 \right). \tag{13}$$

The simple form of Eq. (13) is rather deceptive since the *LHS* of the equation has the magnetic field as a function of the initial proton coordinates x while the *RHS* depends as well on the final proton coordinates x' through $I(x')$, which are in turn coupled through Eq. (8). This being said, we have now obtained a differential equation, Eq. (13), relating the line-integrated B field to the observed proton fluence. For the solution, we regard $I(x')$ and $I_0(x)$ as input data, and integrate to obtain $b(x)$. Numerical solutions are straightforward using ODE solvers, either by hand or using prebuilt packages.

Since Eq. (10) relies on the assumption that deflections are sufficiently weak that $dx'/dx > 0$, the present reconstruction algorithm requires the same condition. This regime was called the "nonlinear injective regime" in Ref. [2]. The regime guarantees that for each proton final position x' the protons arrived from only one x. (Ref. [2] also describes a yet-weaker-deflection regime called the "linear" regime. The present reconstruction technique is also valid in the linear regime.)

Given the structure of Eq. (13), a *unique* reconstruction will be provided by the solution to the equation plus a boundary condition $b_0 = b(x_0)$ at some specified point x_0. Without the boundary condition, the solution is unique up to a uniform offset magnetic field $\bar{b}$ added to the overall solution, which also results in an additional, uniform spatial offset between x and x'. Equivalently, without a specified boundary condition, the reconstruction provides the *relative* change to the magnetic field on the domain. We return to further discussion of boundary conditions below.

We can also calculate the line-integrated current,

$$\int J_z \, dz = \frac{1}{\mu_0} \frac{d}{dx} \int B_y \, dz = \frac{K_B}{\mu_0} \left(\frac{I_0(x)}{I(x')} - 1 \right). \tag{14}$$

This shows the direct relationship between the parallel current density and the proton fluence. The subtlety here again is the mapping $x \rightarrow x'$ so that for a current density at x, the associated proton fluence is observed at x'. This relation is the 1-D analog of equations derived in Ref. [27]. Equation (14) shows the close relationship between the proton fluence and current density, and therefore why an additional integration is needed to obtain the magnetic field, via Eq. (13).

IV. VERIFICATION

We next demonstrate a verification of the reconstruction technique using an example analytic set of fields. We choose a magnetic field profile that is representative of current sheet
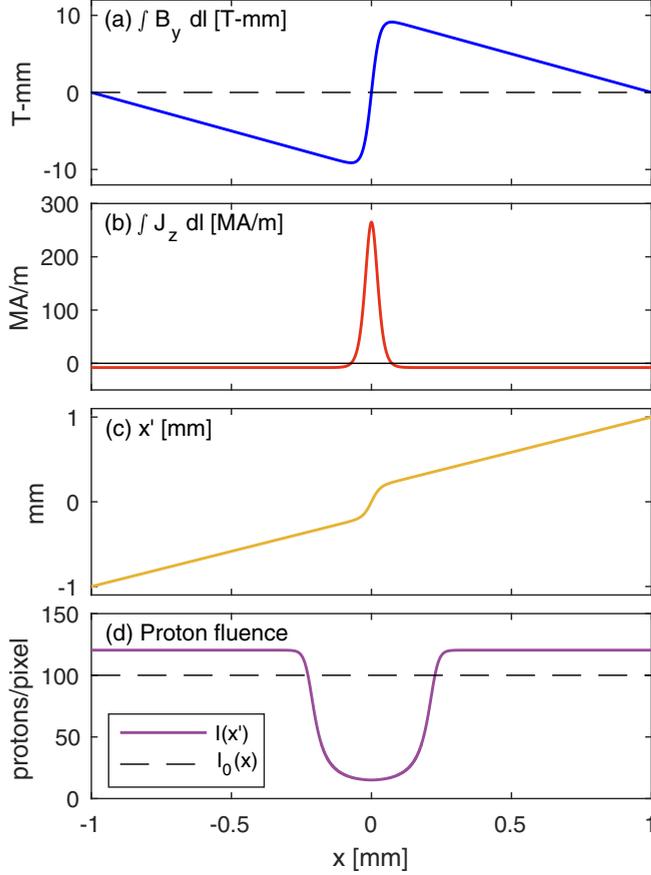
FIG. 2. Analytic profiles for reconstruction verification. (a) Line-integrated magnetic field profile. (b) Plasma current. (c) Proton final position x' for each x. (d) Proton fluence profile.

formation between colliding magnetized plasmas in magnetic reconnection experiments [28]. From the analytic field profiles, we calculate a synthetic proton fluence. This proton fluence is then fed (numerically) into the reconstruction algorithm, and we verify that the reconstruction matches the analytic magnetic field.

We assume a magnetic profile of the form

$$b(x) = b_0 \tanh(x/\delta) \left(1 - \frac{|x|}{L_B} \right). \tag{15}$$

Here, b_0 is the peak (line-integrated) magnetic field which we take as 10 T-mm. L_B is a constant related to the distance to center of each magnetized bubble, which we take as 1 mm, so that the B field returns to zero at $x = \pm L_B$. We will use this formula, and reconstruct, over the domain $x \in [-L_B, L_B]$. Finally, the current sheet width parameter δ is taken as 30 μm. This analytic profile is shown in Fig. 2(a). From this, we calculate a line-integrated plasma current density $\int J_z \, dz = (1/\mu_0) \, d/dx \int B_y \, dz$, shown in Fig. 2(b). The current shows a strong positive spike in the current sheet with a magnitude larger than 250 MA/m. Away from the current sheet, the current density is slightly negative, representing a return current.

We next produce a synthetic set of 1-D proton fluence data, using typical proton parameters from experiments. We take $E_p = 14.7$ MeV, $L_s = 10$ mm, and $L_d = 150$ mm, from
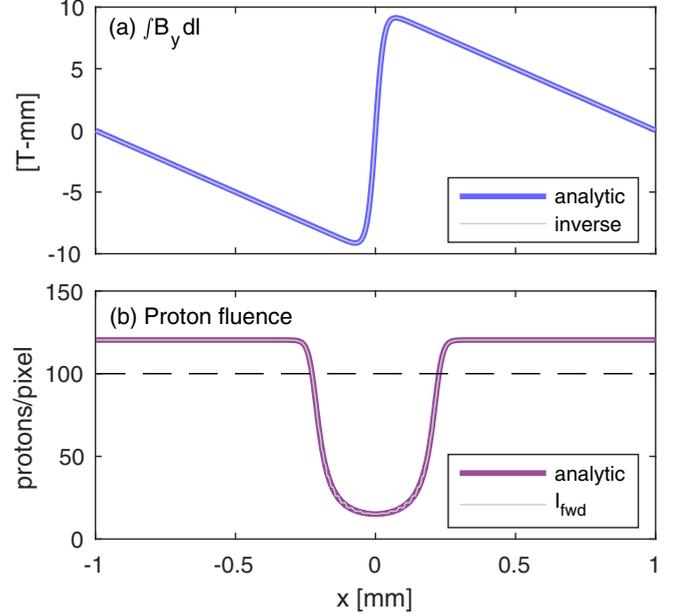
FIG. 3. Reconstruction demonstration. (a) Magnetic field profiles comparing the reconstructed magnetic field with the original analytic form. (b) Proton fluence profiles, comparing the given input proton fluence, and a forward proton model from the reconstructed magnetic field profile I_{fwd}.

which we evaluate $K_B = 59$ T. From this, we calculate proton deflections ξ and accordingly x' as a function of x, which is shown in Fig. 2(c). Finally, we calculate the proton fluence, based on a nominal uniform source proton fluence of I_0 of 100 protons/pixel, shown in Fig. 2(d). The final proton fluence can be calculated semianalytically using the mapping $x \to x'$ and analytic $d\xi/dx$, or numerically by binning the final proton positions. The reversal of the magnetic field causes the protons on opposite sides of the current sheet to diverge (as illustrated in Fig. 1), producing a broad proton fluence depletion near $x = 0$.

This proton fluence profile is then used in the inversion procedure described above, which is to numerically integrate Eq. (13) coupled to Eq. (8). We use the synthetic proton fluence $I(x')$ shown in Fig. 2(d) as input data. Next, at this point, we assume we know the source proton fluence $I_0 = 100$ protons/pixel, and the initial condition on the magnetic field $b = 0$ at $x = -1$ mm, and apply these in the reconstruction. (The reconstruction can equally start at other initial conditions, such as $b = 0$ at $x = +1$ mm; we verified the inversion produces identical reconstructions within the tolerances in each case.)

The results are shown in Fig. 3(a), showing excellent agreement between the analytic profile and the reconstruction. The maximum deviation between the inversion and the analytic B profile is $< 1 \times 10^{-5}$ T-mm, or less than 0.1%.

Finally, as a standard check, we calculate the forward proton fluence I_{fwd} from the reconstruction. The comparison of I_{fwd} with the input data $I(x')$ is a useful (and minimal) test for the general case when there is no analytic magnetic field to compare against. To do so, we numerically calculate ξ based on the reconstructed field and bin the final proton

positions, shown in Fig. 3(b). The agreement with the original input $I(x')$ is excellent, which is to be expected since we also had agreement between the analytical and reconstructed fields. Some fine-scaled "jaggedness" can be observed in I_{fwd}, which is due to the finite spatial resolution of the reconstruction. The maximum difference between I_{fwd} and the synthetic input data was <2.5 protons/pixel, and the RMS deviation was <0.5 protons/pixel. These results illustrate the overall numerical verification of this 1-D reconstruction technique.

V. BOUNDARY CONDITIONS AND THE SOURCE FLUENCE I_0

We now study how the source proton fluence and boundary conditions can impact 1-D magnetic reconstructions. In this section, we develop the relationship between these quantities and how uncertainties in these quantities feed through to results of the reconstruction.

For the reconstruction above (Fig. 3), we assumed we knew two important quantities: the initial condition to start the integration from, and the source proton fluence $I_0(x)$. Solutions of Eq. (13) can add a uniform magnetic field, which leads to a constant additional offset of x and x', So, without a specified boundary condition, only the relative change of the field across the integration domain is obtained from the analysis. For some applications, such as observing the RMS or fluctuating components of the magnetic field (e.g., Refs. [2,14]), the relative variations may be sufficient. However, other contexts, such as for magnetic reconnection or collisionless shock experiments, the absolute magnitude may be very important.

Next, the source fluence I_0 is also required for the reconstruction. In the example above, we posited that we knew the source fluence $I_0(x) = 100$ protons/pixel. However, we now conduct an exercise imagining that there was some uncertainty in determining this quantity. Figure 4 shows the results for reconstructing the same $I(x')$ above but with I_0 now set at 90 or 110 protons/pixel (still uniform on the domain). The resulting reconstructed fields are shown in Fig. 4(a), as the dashed and dot-dashed curves, labeled with the associated I_0. We observe that this change in I_0 leads to significantly different reconstructed magnetic fields. Roughly speaking, the change in I_0 introduces a positive or negative ramp to $b(x)$, which we will call the "integration error." The magnetic field still makes a similar jump in each case, yet the position of the jump is offset, due to the error propagated through the mapping $x \rightarrow x'$. By the right-hand boundary, the curves have significantly different magnitudes, yielding $b(x)$ near ± 10 T-mm, which is approximately equal to the *maximum* value $b_{\max}$ from the $I_0 = 100$ solution. It is clear that $|\delta b|/|b_{\max}| \sim 100\%$, where δb is the difference between solutions.

Additionally, Fig. 4(b) shows the associated reconstructed current density. We see that the location of the peak currents are offset spatially, just like the spatial offsets of the magnetic field jumps. However, the *peak* currents are actually fairly similar ($\pm 10\%$). This indicates that some outputs from an analysis, such as peak current, can be more robust to I_0 errors than magnetic field measurements.
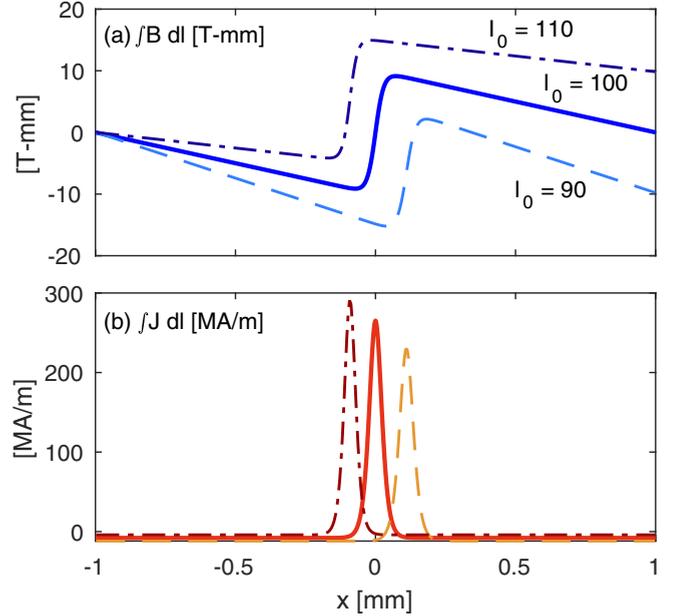
FIG. 4. Proton reconstructions under multiple values of I_0. (a) Magnetic field calculations for uniform $I_0 = 90$, 100, and 110 protons/pixel as labeled. (b) Associated plasma current density reconstructions.

We now characterize the ramp ("integration error") resulting from an error in I_0. We return to Eq. (13) and introduce an error in the source fluence measurement δI_0. We obtain

$$\frac{db}{dx} = K_B\left(\frac{I_0}{I(x')} + \frac{\delta I_0}{I(x')} - 1\right). \qquad (16)$$

While this equation is complicated, owing again to the nonlinear dependence of $I(x')$ on x', we can see immediately that adding a δI_0 upsets the balance between I_0 and I, leading to a net positive or negative accumulation to the integral.

We now consider the most simple case, assuming $I = I_0 = $ const [so that the nominal $b(x) = $ constant as well], and again introduce δI_0. This case can be solved directly for the integration error δb, and we obtain

$$\delta b = K_B \int \frac{\delta I_0}{I_0}\, dx = K_B \frac{\delta I_0}{I_0}\Delta x, \qquad (17)$$

where Δx is the integration distance. This shows that δI_0 produces an integration error δb which accumulates in space, with slope $K_B \delta I_0 / I_0$. This result matches with the numerical example in Fig. 4(a): taking $K_B = 59$ T, $\delta I_0/I = 10\%$, and $\Delta x = 2$ mm, we get an accumulated δb error $\approx$12 T-mm. Therefore, this explains the overall positive and negative slopes introduced by δI_0. Note that further features will also be introduced in the general case, such as the spatial offsets of where the magnetic jump occurs in Fig. 4(a), produced by the additional nonlinearity of the proton mapping.

This result directly connects magnetic field measurement errors to errors in I_0. Similar classes of "integration errors" are common in other fields, such as electronic integration circuits, whenever small but correlated offset errors integrate to produce spurious signals. This issue illustrates a challenge of reconstructing magnetic fields from proton fluence measurements. We note that this issue generalizes to input proton

fluence *nonuniformities* [i.e., an x-dependence of $I_0(x)$]. Such nonuniformities, if not characterized and accounted for in the analysis, also integrate up to produce spurious magnetic fields. This effect is worse at long wavelengths, and for longer integration domains ($\delta b \propto \Delta x$).

VI. BOUNDARY-CONSTRAINED RECONSTRUCTION

The previous section showed how different I_0 can produce significantly different reconstructions, and specifically how the changes to the average $\bar{I}_0$ leads to different ramp rates of the magnetic field across the domain. Accordingly, it is important to constrain this quantity for experimental analysis. In this section, we develop a *boundary-constrained* reconstruction that uses a pair of boundary conditions on the magnetic field, which yields a reconstruction that passes through both specified boundary conditions, and in the process infers the required average $\bar{I}_0$.

We recall that Fig. 4 shows that using different I_0 produces a large family of magnetic field solutions which ramp to nearly arbitrary values elsewhere in the domain. However, the converse is also true: *if the magnetic field boundary conditions are specified at multiple points, then I_0 can be chosen so that the reconstructed field passes through those points.* There is a relationship between I_0 and the boundary conditions on $b(x)$.

We now directly construct this, using the principle of conservation of protons: imagine that we specify a *two-point* boundary condition on $b(x)$, namely $b(x_1) = b_1$ and $b(x_2) = b_2$. Then we can calculate $x_1' = x_1 + b_1/K_B$ and $x_2' = x_2 + b_2/K_B$. From this we integrate the total protons landing between x_1' and x_2', which is $\int_{x_1'}^{x_2'} I(x')\,dx'$. This determines $\bar{I}_0$, which is the average of I_0 on $[x_1, x_2]$, via

$$\int_{x_1'}^{x_2'} I(x')\,dx' = \int_{x_1}^{x_2} I_0(x)\,dx \equiv \bar{I}_0 \Delta x, \tag{18}$$

where $\Delta x = x_2 - x_1$ is the integration distance. Therefore, *a two-point boundary condition on the magnetic field is sufficient to fix the average of the input proton fluence $\bar{I}_0$.* This relation is exact, even considering the nonlinearity of the mapping.

We now implement this new prescription for a final set of reconstructions, shown in Fig. 5, where we take that I_0 is unknown before the analysis but specify two-point boundary conditions on $b(x)$. We run two cases, one where we use the previous $b_{bc} = 0$ at $x_{bc} = \pm 1$ mm, exactly as analyzed in Fig. 3, and a case where $(x, b)_{bc}$ are $(-1 \text{ mm}, -10 \text{ T-mm})$ and $(+1 \text{ mm}, +10 \text{ T-mm})$, which we call the ± 10 T-mm case.

The boundary information is used to infer $\bar{I}_0$ for each case, via Eq. (18), which is then used to reconstruct the magnetic fields. (We again use a uniform $I_0 = \bar{I}_0$ for each case.) For the $b_{bc} = 0$ case, I_0 is inferred to be exactly 100 protons/pixel (as expected). For the $b_{bc} = \pm 10$ T-mm case, I_0 is inferred to be 120.4 protons/pixel. The results are shown in Fig. 5(a), with the dark blue curve showing the solution for $b_{bc} = 0$, and the light blue dashed curve showing the solution for $b_{bc} = \pm 10$ T-mm. We observe that the magnetic field exactly achieves the specified boundary conditions in each case.

Finally, Fig. 5(b) shows a plot of inferred line-integrated current density $\int J_z\,dz$ for each case, zoomed to a smaller domain near the current sheet. We observe that the shapes are quantitatively similar, but there is a $\approx 20\%$ difference in the
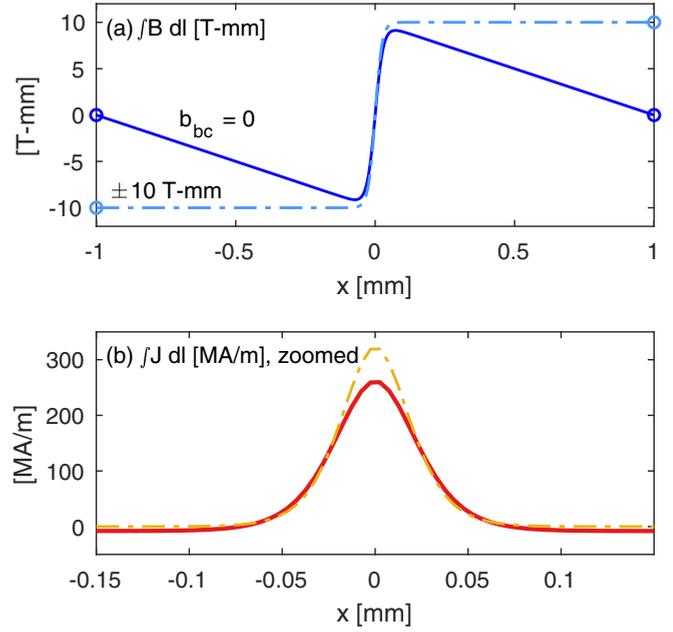
FIG. 5. Demonstration of radiography reconstructions to achieve specified boundary conditions, where $\bar{I}_0$ is considered a free parameter. (a) Reconstruction of line-integrated magnetic field to achieve $b_{bc} = 0$ (dark blue), or $b_{bc} = \pm 10$ T-mm (light blue, dashed) at the two ends of the domain. (b) Current profiles determined for each case, where the red curve is the $b_{bc} = 0$ case and the yellow dashed curve is for the $b_{bc} = \pm 10$ T-mm case.

peak current density, due to the difference in I_0 determined for each case. The fractional difference in $\int J_z\,dz$ is due to the difference $\delta I_0/I_0 \approx 20\%$ between the cases.

To conclude, in this section, we developed a boundary-constrained reconstruction procedure, which reconstructs a magnetic field profile matching a pair of magnetic field boundary conditions (x_1, b_1) and (x_2, b_2). As shown in Fig. 5, given different boundary conditions, different reconstructed field profiles can be generated, even from the same observed proton fluence profile $I(x')$. The difference comes in through a different inferred (average) source fluence $\bar{I}_0$ for each case. These results highlight the general importance of applying boundary condition information for reconstruction analysis, as well as the interrelation between boundary conditions and the source proton fluence.

A final point is that the source proton fluence may not be perfectly uniform. The discussion here shows that the magnetic field boundary conditions will constrain the average of the input proton fluence. However, it may still be clear in the raw data that additional "structure" and spatial dependence of the proton fluence $I_0(x)$ should be accounted for. In general, additional information will be needed to constrain structure of the source fluence. Some statistical strategies for nonuniform fluence profiles have been discussed in Ref. [25]. We leave this to be pursued on a case-by-case basis, and for future publications which focus primarily on experimental data.

VII. RECONSTRUCTION WITH EXPERIMENTAL DATA

We conclude with an example reconstruction using data from magnetic reconnection experiments from the National

Ignition Facility [26]. The goal of this section is to show a demonstration reconstruction of raw experimental data and the importance of boundary conditions. Here we show a "hybrid" proton deflectometry scheme with mesh and fluence reconstruction regions, which allows us to directly implement the boundary-constrained analysis of Sec. VI to complete a reconstruction with experimentally determined boundary conditions.

In the experiments, two separate plumes are produced by multiple lasers irradiating a solid carbon target. The expanding plumes self-magnetize through the Biermann battery effect, which produces a toroidal field wrapping around each plume [6]. Subsequent collision of the two plumes compresses the opposite fields from the two plumes and drives magnetic reconnection [9–12]. Measuring magnetic fields in the experiments is valuable to address scientific goals such as understanding the structure of the current sheet, growth of instabilities, and quantities such as the upstream magnetic fields, plasma current density, the width of the current sheet, and rate of magnetic reconnection [28–30] which can be compared against magnetic reconnection models and observations from space and astrophysical plasmas [31].

The experimental geometry is very similar to Fig. 1 and is shown schematically in Fig. 6. To achieve the quasi-1-D geometry, two lines of 20 laser beams were tiled onto a flat target occupying the (x, y) plane. The laser foci were in two groups focused at $x = \pm 1.2$ mm, with each group tiled in the y-direction over 4 mm, producing two highly elongated plumes. The two plumes collided at $x = 0$, producing a quasi-1-D current sheet. The peak, overlapped laser intensity on-target was $I_L = 1 \times 10^{14}$ W/cm^2, with a 0.6 ns square pulse. The beams were all in the group of "outer" beams at NIF which had on-target angles of 44°–50°, and used phase plates designed to focus to a circular focal spot in the horizontal plane of the target with FWHM 1.24–1.28 mm. The calculated intensity profile is shown in Fig. 6(c). A D^{3}He backlighter was imploded by separate drive beams a distance $L_s = 20$ mm away from the foil. A detector stack was mounted a distance $L_d = 222$ mm on the opposite side. The data from 3 and 14.7 MeV protons was registered on CR-39 proton-track detectors and scanned by standard techniques [32].

We attached laser-cut meshes (Au, thickness 76 μm) to the back of the target over some regions to break the protons into beamlets. Tracking the beamlet deflections provides a direct magnetic field measurement at these locations via Eq. (8). In addition to the CR-39 detectors, the detector stack also included an image plate (IP), positioned after the 14.7 MeV CR-39 which measured x rays produced by the D^{3}He implosion. The IP records the x-ray shadow of the mesh, which provides the absolute reference location for each beamlet [15,16]. Filtering through the stack provides a low-energy cutoff of $h\nu \gtrsim 25$ keV for the x rays reaching the IP. The IP and CR-39s were co-aligned to better than 0.5 pixel in postprocessing analysis using the toothed features at the image boundary, imprinted by a fiducial frame at the front of the detector stack.

Figure 7(a) shows a raw 14.7 MeV proton radiograph from the experiment. The backlighter was timed such that the 14.7 MeV protons crossed the plasma plane 3.0 ns after the start of the main laser drive. Meshes (indicated by 'A' and 'C') were
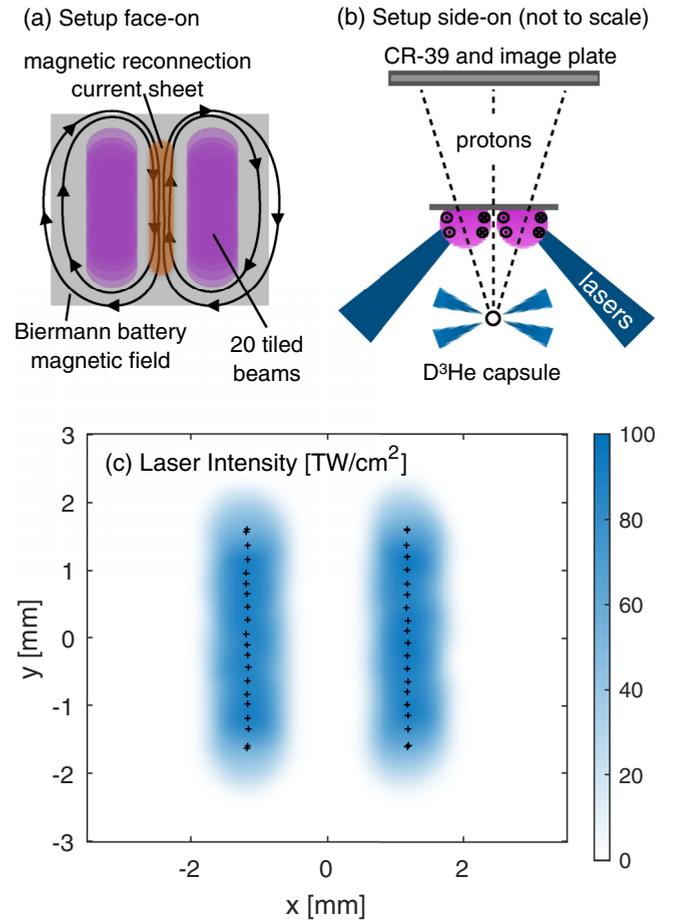
FIG. 6. Experimental setup at NIF. (a) Schematic of the laser profile on-target, Biermann battery magnetic fields, and current sheet. (b) Schematic side-on view of the target including a D^{3}He capsule and detector stack (not to scale). (c) Laser intensity profile on-target from two sets of 20 tiled laser beams. Individual laser foci are indicated as the crossed data points.

used on the nonreconnecting sides of the plumes, whereas the mesh-free region ('B') in the reconnection region allows for a magnetic field reconstruction. The footprints of the two groups of drive lasers are indicated by the red ovals centered at $x = \pm 1.2$ mm, which are extended along y by tiling the lasers, and denote the centroid of each plume. Two high-proton-fluence (dark) bands, visible in region B, are produced by the toroidal Biermann-battery fields wrapping around each plume. The two plumes collide to produce a reconnection current sheet which is observed as a low-fluence (light) region centered at $x = 0$. The magnetic field in the current sheet region is quasi-1-D, allowing the 1-D analysis developed in this work.

The proton fluence profile along x is plotted in Fig. 7(b) and shown as the purple curve. In regions A and C, the mesh modulation is visible. Region B provides the proton fluence data from the central current sheet region. The fluence profile plotted in Fig. 7(b) is obtained by averaging over $y \in [-1, 1]$ mm. The raw fluence data shows qualitative agreement with the analytic profiles in Fig. 2(d), especially the broad fluence
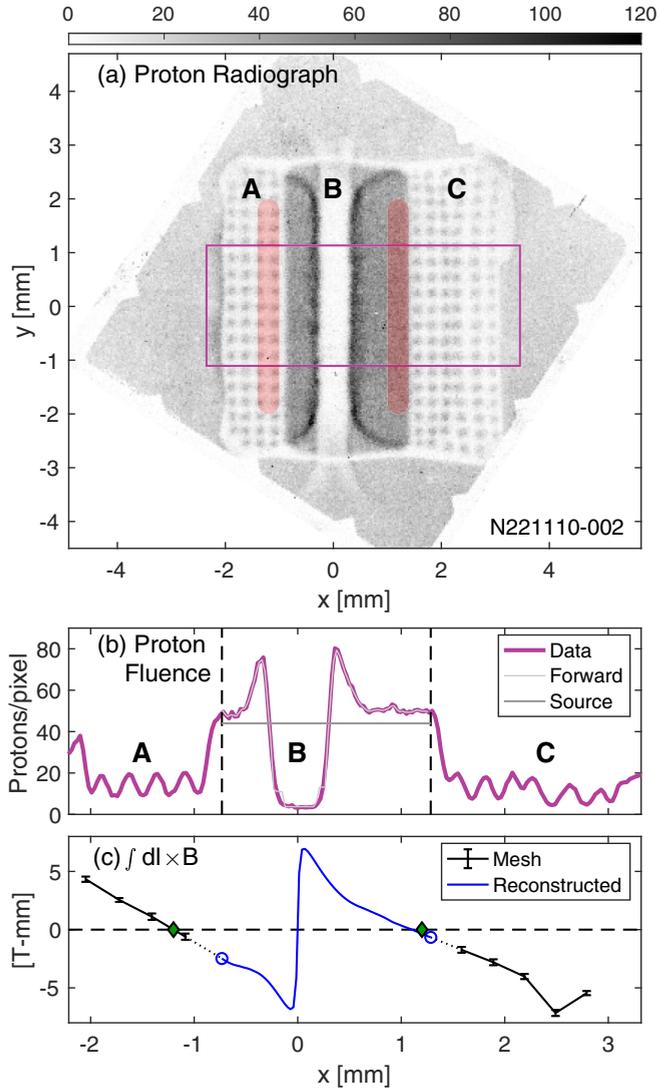
FIG. 7. Proton radiography data from magnetic reconnection experiments at NIF and associated magnetic field reconstructions. (a) Raw proton radiograph image, containing both mesh regions 'A' and 'C' and a mesh-free region 'B' for fluence analysis. The footprints of the drive laser groups are indicated as light red ovals. (b) Profile of the proton fluence data (purple) over the purple box from (a), averaged in the y-direction. These data were used to reconstruct the field in panel (c). The dark gray line indicates the inferred source proton fluence, and the light gray line indicates the forward model proton fluence from the reconstruction. (c) Direct measurements of $\int B_y\,dz$ (black points with error bars) from mesh data and reconstructed $\int B_y\,dz$ from the proton fluence data (blue). Boundary conditions for the reconstruction are indicated by the blue circles at the ends of the reconstructed curve and were determined from extrapolating the mesh data. Green diamonds indicate the centers of the laser foci at $x = \pm 1.2$ mm where $\int B_y\,dz = 0$ is expected by symmetry.

depletion near $x = 0$, indicating the current sheet where the magnetic field rapidly reverses.

Figure 7(c) shows the magnetic field reconstructed from this fluence data. We apply the boundary-constrained reconstruction developed in Sec. VI. The boundary conditions for

the magnetic field were obtained from the mesh data. The deflection of each beamlet from its reference location was obtained by comparing the beamlet data between the 14.7 MeV proton and the IP x-ray data [15,16]. This directly provides the magnetic field at each beamlet, plotted as the black data points in Fig. 7(c), where the error bars indicate the standard deviation within each column. Since the first mesh cell is some distance into the mesh region, we extrapolated the boundary condition linearly from the two nearest mesh points to the first available point in the fluence region. These points are shown in Fig. 7(c) as the blue circles at the ends of the magnetic field reconstruction. The magnetic field is then reconstructed from the fluence data, shown as the blue curve. The raw proton fluence did not show strong evidence that the source' proton fluence was nonuniform, so we reconstructed with a uniform source fluence, with the fluence level inferred from the boundary-constraint analysis from Sec. VI, shown as the light gray line in Fig. 7(b). The magnetic field profile has a qualitatively similar shape to the prior analytic examples, with the peak line-integrated magnetic field strength near 7 T-mm. The nominal centers of the laser foci for each plume are indicated as green diamonds at $x = \pm 1.2$ mm, and we observe that the inferred magnetic field crosses through zero near these points, as expected by the symmetry of the Biermann-battery field-generation process.

As a final check, the reconstructed magnetic field profile was used to generate the forward model proton fluence, plotted as the thin gray curve in Fig. 7(b), which is seen to be in good agreement with the raw proton data. Some fine-scale jaggedness in the data is observed in the current sheet, which is a result of the finite spatial resolution of the proton data (equivalent to 28 μm in the plasma plane). We always apply this check to verify a minimum of agreement between the inferred magnetic field and the data.

VIII. DISCUSSION AND CONCLUSIONS

A 1-D reconstruction procedure was developed to infer electromagnetic fields in high-energy-density plasma experiments. A 1-D reconstruction is valuable as a complement and cross-check to 2-D analyses and may be directly applied to 1-D experiments. Here we verified the 1-D reconstruction algorithm against semianalytical field models, and presented an example showing that it can reconstruct magnetic field data from a recent experiment at NIF. The software package PRADICAMENT was developed that implements this algorithm and is discussed in the Appendix.

Using the algorithm, we then explored the relation between the boundary conditions and source fluence for 1-D reconstructions. First, we showed that proton fluence measurements are closely related to plasma current measurements, which is why an integration is required to infer the magnetic fields from the proton fluence. A boundary condition is needed to obtain the absolute magnetic field, as otherwise the analysis produces only the relative change of the magnetic field across the domain. Second, we showed that if there are errors or uncertainties in characterizing source proton fluence, then this leads to "integration errors" in reconstructing the magnetic field, which increases with the length of the reconstructed domain. However, we showed that applying *two-point* boundary

conditions on the magnetic field (x_1, b_1), and (x_2, b_2), can be used to fix the average source proton fluence on the interval $[x_1, x_2]$, and from this we developed a boundary-constrained reconstruction in Sec. VI.

From these considerations, we conclude that boundary conditions can be critical input data to the analysis. It is obviously a best practice to directly confirm the boundary conditions with experimental measurements. To do so, we developed a "hybrid" proton deflectometry technique, which combines fluence analysis with boundary conditions from beamlet mapping [15,16]. The direct magnetic field measurements from the beamlet analysis were used as boundary conditions to constrain a high-resolution fluence reconstruction in Sec. VII.

The present 1-D algorithm has some valuable complementary features compared to Monge-Ampère-type reconstruction implementations (e.g., Ref. [2]). While not developed extensively here, it is also possible to run the present algorithm in a "free-boundary" mode. This mode takes as input the observed fluence $I(x')$ and a specified source fluence $I_0(x)$, and produces a reconstructed magnetic field. With no boundary conditions applied, one should remember that this mode only produces the relative change of the magnetic field over the domain, and one should test the sensitivity of the results to uncertainty in I_0. Nevertheless, this technique could also be useful under certain circumstances, and especially for "short-baseline" reconstructions where there is not a long distance for integration errors to pile up; in contrast, the Monge-Ampère-type relaxation solvers always produce a magnetic field with fixed boundary conditions (with commonly used reconstruction codes using $\mathbf{B}_{\text{tangential}} = 0$, as of the time of this writing [24]).

Since the goal of this work has been to demonstrate the overall reconstruction procedure, we defer detailed error analysis to future publications, but one can imagine that several sources of error can be incorporated, including the uncertainty in boundary conditions, finite spatial resolution effects, fluence background, and nonuniformity in the source proton fluence. For the present data, it appeared that the source proton fluence was relatively flat, so we used a flat source fluence profile for the simplest possible reconstruction; however, future work will consider constraining nonuniformity in the source fluence as part of the analysis, and how this feeds into uncertainty in the final reconstructed magnetic field. Once again, having the ground truth of direct magnetic field data at several points will form an important constraint on the final profiles.

APPENDIX: RECONSTRUCTION CODE AND AVAILABILITY

The algorithms above have been implemented in Matlab and are available in a package called PRADICAMENT on GitHub at [33].

The code works in the consistent unit scheme described near Eqs. (6) and (7). In other words, if K_B is in T and spatial units are in m, then $b(x)$ will be in T-m. If $K_B = 1$ is specified, then the value returned from the reconstructions will be $\xi(x)$ rather than $b(x)$. If K_E is used rather than K_B, then the values returned will be line-integrated electric fields. The spatial coordinates are that of the plasma plane, as described near Eq. (8).

The main routines, as of v1.0, are as follows:

(1) `prad_inv` — proton-radiography inverse solver in 1-D, using specified boundary conditions. It takes as input data proton fluence I and I_0, K_B, and a required boundary condition pair (x_1, b_1), and (x_2, b_2). I_0 provides only the overall shape, since it is first renormalized to achieve the specified boundary conditions on $b(x)$, per Eq. (18).

(2) `prad_inv_I0` — proton-radiography inverse solver in 1-D, using a specified I_0. It takes as input data I and I_0 as a function of coordinate x, along with a specified K_B, and an optional (x_0, B_0) pair to initiate the integration. It integrates Eq. (13) coupled to Eq. (8), using standard ODE solvers. The routine interpolates I and I_0 between values at the specified mesh points as needed.

(3) `prad_fwd` — produces a forward model proton image $I_{\text{fwd}}(x)$ from a given magnetic field profile $b(x)$. It launches a large number off synthetic protons which are sent through the mapping and binned to final positions. Because it uses binning, it correctly produces the proton image even in caustic regimes. Required inputs are $I_0(x)$, $b(x)$, and K_B.

[1] N. L. Kugland, D. D. Ryutov, C. Plechaty, J. S. Ross, and H. S. Park, Invited article: Relation between electric and magnetic field structures and their proton-beam images, Rev. Sci. Instrum. **83**, 101301 (2012).

[2] A. F. A. Bott, C. Graziani, P. Tzeferacos, T. G. White, D. Q. Lamb, G. Gregori, and A. A. Schekochihin, Proton imaging of stochastic magnetic fields, J. Plasma Phys. **83**, 905830614 (2017).

[3] D. B. Schaeffer, A. F. A. Bott, M. Borghesi, K. A. Flippo, W. Fox, J. Fuchs, C. Li, F. H. Séguin, H.-S. Park, P. Tzeferacos, and L. Willingale, Proton imaging of high-energy-density laboratory plasmas, Rev. Mod. Phys. **95**, 045007 (2023).

[4] O. V. Gotchev, P. Y. Chang, J. P. Knauer, D. D. Meyerhofer, O. Polomarov, J. Frenje, C. K. Li, M. J.-E. Manuel, R. D. Petrasso, J. R. Rygg, F. H. Séguin, and R. Betti, Laser-driven magnetic-flux compression in high-energy-density plasmas, Phys. Rev. Lett. **103**, 215004 (2009).

[5] C. K. Li, F. H. Séguin, J. A. Frenje, J. R. Rygg, R. D. Petrasso, R. P. J. Town, P. A. Amendt, S. P. Hatchett, O. L. Landen, A. J. Mackinnon, P. K. Patel, V. A. Smalyuk, T. C. Sangster, and J. P. Knauer, Measuring E and B fields in laser-produced plasmas

with monoenergetic proton radiography, Phys. Rev. Lett. **97**, 135003 (2006).

[6] R. D. Petrasso, C. K. Li, F. H. Seguin, J. R. Rygg, J. A. Frenje, R. Betti, J. P. Knauer, D. D. Meyerhofer, P. A. Amendt, D. H. Froula, O. L. Landen, P. K. Patel, J. S. Ross, and R. P. J. Town, Lorentz mapping of magnetic fields in hot dense plasmas, Phys. Rev. Lett. **103**, 085001 (2009).

[7] L. Gao, P. M. Nilson, I. V. Igumenshchev, M. G. Haines, D. H. Froula, R. Betti, and D. D. Meyerhofer, Precision mapping of laser-driven magnetic fields and their evolution in high-energy-density plasmas, Phys. Rev. Lett. **114**, 215003 (2015).

[8] W. Fox, G. Fiksel, A. Bhattacharjee, P. Y. Chang, K. Germaschewski, S. X. Hu, and P. M. Nilson, Filamentation instability of counterstreaming laser-driven plasmas, Phys. Rev. Lett. **111**, 225002 (2013).

[9] P. M. Nilson, L. Willingale, M. C. Kaluza, C. Kamperidis, S. Minardi, M. S. Wei, P. Fernandes, M. Notley, S. Bandyopadhyay, M. Sherlock, R. J. Kingham, M. Tatarakis, Z. Najmudin, W. Rozmus, R. G. Evans, M. G. Haines, A. E. Dangor, and K. Krushelnick, Magnetic reconnection and plasma dynamics in two-beam laser-solid interactions, Phys. Rev. Lett. **97**, 255001 (2006).

[10] C. K. Li, F. H. Séguin, J. A. Frenje, J. R. Rygg, R. D. Petrasso, R. P. J. Town, O. L. Landen, J. P. Knauer, and V. A. Smalyuk, Observation of megagauss-field topology changes due to magnetic reconnection in laser-produced plasmas, Phys. Rev. Lett. **99**, 055001 (2007).

[11] G. Fiksel, W. Fox, A. Bhattacharjee, D. H. Barnak, P. Y. Chang, K. Germaschewski, S. X. Hu, and P. M. Nilson, Magnetic reconnection between colliding magnetized laser-produced plasma plumes, Phys. Rev. Lett. **113**, 105003 (2014).

[12] M. J. Rosenberg, C. K. Li, W. Fox, A. B. Zylstra, C. Stoeckl, F. H. Séguin, J. A. Frenje, and R. D. Petrasso, Slowing of magnetic reconnection concurrent with weakening plasma inflows and increasing collisionality in strongly driven laser-plasma experiments, Phys. Rev. Lett. **114**, 205004 (2015).

[13] D. B. Schaeffer, W. Fox, R. K. Follett, G. Fiksel, C. K. Li, J. Matteucci, A. Bhattacharjee, and K. Germaschewski, Direct observations of particle dynamics in magnetized collisionless shock precursors in laser-produced plasmas, Phys. Rev. Lett. **122**, 245001 (2019).

[14] P. Tzeferacos *et al.*, Laboratory evidence of dynamo amplification of magnetic fields in a turbulent plasma, Nat. Commun. **9**, 591 (2018).

[15] C. L. Johnson, S. Malko, W. Fox, D. B. Schaeffer, G. Fiksel, P. J. Adrian, G. D. Sutcliffe, and A. Birkel, Proton deflectometry with *in situ* x-ray reference for absolute measurement of electromagnetic fields in high-energy-density plasmas, Rev. Sci. Instrum. **93**, 023502 (2022).

[16] S. Malko, C. Johnson, D. B. Schaeffer, W. Fox, and G. Fiksel, Design of proton deflectometry with *in situ* x-ray fiducial for magnetized high-energy-density systems, Appl. Opt. **61**, C133 (2022).

[17] M. F. Kasim, L. Ceurvorst, N. Ratan, J. Sadler, N. Chen, A. Sävert, R. Trines, R. Bingham, P. N. Burrows, M. C. Kaluza, and P. Norreys, Quantitative shadowgraphy and proton

radiography for large intensity modulations, Phys. Rev. E **95**, 023306 (2017).

[18] J. Davies, P. Heuer, and A. Bott, Quantitative proton radiography and shadowgraphy for arbitrary intensities, High Energ. Dens. Phys. **49**, 101067 (2023).

[19] M. M. Sulman, J. Williams, and R. D. Russell, An efficient approach for the numerical solution of the Monge–Ampère equation, Appl. Numer. Math. **61**, 298 (2011).

[20] N. F. Y. Chen, M. F. Kasim, L. Ceurvorst, N. Ratan, J. Sadler, M. C. Levy, R. Trines, R. Bingham, and P. Norreys, Machine learning applied to proton radiography of high-energy-density plasmas, Phys. Rev. E **95**, 043305 (2017).

[21] C. A. Walsh, J. P. Chittenden, D. W. Hill, and C. Ridgers, Extended-magnetohydrodynamics in under-dense plasmas, Phys. Plasmas **27**, 022103 (2020).

[22] M. R. Gomez *et al.*, Performance scaling in magnetized liner inertial fusion experiments, Phys. Rev. Lett. **125**, 155002 (2020).

[23] P. T. Campbell, C. A. Walsh, B. K. Russell, J. P. Chittenden, A. Crilly, G. Fiksel, P. M. Nilson, A. G. R. Thomas, K. Krushelnick, and L. Willingale, Magnetic signatures of radiation-driven double ablation fronts, Phys. Rev. Lett. **125**, 145001 (2020).

[24] The PROBLEM reconstruction code, https://github.com/flash-center/PROBLEM.

[25] M. F. Kasim, A. F. A. Bott, P. Tzeferacos, D. Q. Lamb, G. Gregori, and S. M. Vinko, Retrieving fields from proton radiography without source profiles, Phys. Rev. E **100**, 033208 (2019).

[26] W. Fox, D. Schaeffer, M. Rosenberg, G. Fiksel, J. Matteucci, H.-S. Park, A. Bott, K. Lezhnin, A. Bhattacharjee, D. Kalantar, B. Remington, D. Uzdensky, C. Li, F. Séguin, and S. Hu, Fast magnetic reconnection in highly-extended current sheets at the National Ignition Facility, arXiv:2003.06351.

[27] C. Graziani, P. Tzeferacos, D. Q. Lamb, and C. Li, Inferring morphology and strength of magnetic fields from proton radiographs, Rev. Sci. Instrum. **88**, 123507 (2017).

[28] W. Fox, A. Bhattacharjee, and K. Germaschewski, Fast magnetic reconnection in laser-produced plasma bubbles, Phys. Rev. Lett. **106**, 215003 (2011).

[29] W. Fox, A. Bhattacharjee, and K. Germaschewski, Magnetic reconnection in high-energy-density laser-produced plasmas, Phys. Plasmas **19**, 056309 (2012).

[30] K. V. Lezhnin, W. Fox, J. Matteucci, D. B. Schaeffer, A. Bhattacharjee, M. J. Rosenberg, and K. Germaschewski, Regimes of magnetic reconnection in colliding laser-produced magnetized plasma bubbles, Phys. Plasmas **25**, 093105 (2018).

[31] M. Yamada, R. Kulsrud, and H. Ji, Magnetic reconnection, Rev. Mod. Phys. **82**, 603 (2010).

[32] F. H. Séguin, J. A. Frenje, C. K. Li, D. G. Hicks, S. Kurebayashi, J. R. Rygg, B.-E. Schwartz, R. D. Petrasso, S. Roberts, J. M. Soures, D. D. Meyerhofer, T. C. Sangster, J. P. Knauer, C. Sorce, V. Y. Glebov, C. Stoeckl, T. W. Phillips, R. J. Leeper, K. Fletcher, and S. Padalino, Spectrometry of charged particles from inertial-confinement-fusion plasmas, Rev. Sci. Instrum. **74**, 975 (2003).

[33] https://github.com/wrfox/PRADICAMENT.